Alternative method for differential phase-contrast imaging with weakly coherent hard x rays

Zhi-Feng Huang,[*] Ke-Jun Kang, Li Zhang, Zhi-Qiang Chen, Fei Ding, Zhen-Tian Wang, and Qiao-Guang Fang
Department of Engineering Physics, Tsinghua University, Beijing, 100084, China
and Key Laboratory of Particle & Radiation Imaging (Tsinghua University), Ministry of Education, Beijing, 100084, China

(Received 1 April 2008; revised manuscript received 3 July 2008; published 16 January 2009)

Hard x-ray phase-contrast imaging provides high sensitivity to weakly absorbing low-Z objects in medicine, biology, and materials science. Here, we describe a feasible method to obtain differential phase-contrast images directly with incoherent x-ray sources, avoiding the Talbot effect, which requires coherent x rays. This method was validated experimentally on material and biological samples, and the results prove that differential phase-contrast imaging can be realized under more relaxed conditions. It also demonstrates the feasibility of phase-contrast imaging with conventional x-ray tubes, and should benefit clinical diagnoses, biological examinations, and material inspections in the near future.

DOI: 10.1103/PhysRevA.79.013815 PACS number(s): 42.30.Va, 41.50.+h, 87.59.−e

I. INTRODUCTION

Conventional hard x-ray imaging generates image contrast by reason of variations in x-ray attenuation that arises from absorption and scattering of imaged objects. However, weakly absorbing low-Z objects have such poor contrast that their internal structures cannot be distinguished easily despite increasing doses. In general, for x rays, the complex refractive index of an object can be expressed as $n=1-\delta-i\beta$, where the refractive index decrement δ determines the phase shift ϕ of the x rays passing through the object. The absorption index β is correlated with the linear absorption coefficient μ [1]. Actually, δ is 1000 times larger than β [2]. If ϕ can be measured, then δ (i.e., n) can be calculated. Since the 1990s, several hard x-ray phase-contrast imaging methods have been developed to achieve this aim. Interferometer-based methods use an x-ray interferometer to measure ϕ directly [3]. Propagation-based methods apply Fresnel diffraction to provide contrast relative to the second derivative of the phase shift, $\nabla^2\phi$ [4–6]. Analyzer-based methods yield a differential phase shift $\nabla\phi$ by use of a perfect crystal according to Bragg diffraction theory [7–10]. Grating-based methods also obtain $\nabla\phi$ by use of Talbot interferometry [11–15]. The above methods all rely on the high coherence of synchrotron radiation sources or microfocus x-ray tubes.

The requirement for coherence is the main obstacle to clinical diagnosis of phase-contrast imaging because current medical x-ray imaging equipment employs conventional x-ray tubes, providing weakly coherent x rays. Fortunately, Pfeiffer *et al.* first attempted to measure the differential phase shift by use of a Talbot-Lau interferometer with a conventional x-ray tube in 2006 [16–18]. The Talbot-Lau interferometer can be regarded as a combination of a source grating and a Talbot interferometer. The source grating acts as a beam splitter to create an array of line sources providing individually partially spatial coherent x rays to irradiate tested objects. Then phase-shift gradients are measured by Talbot interferometry. The key idea behind this method is that weakly coherent x rays from conventional x-ray tubes are changed into partially coherent x rays by the source grating, and then interferometric methods are adopted to measure phase-shift gradients.

Thus, partially coherent x rays and interferometric measurements have been essential to hard x-ray phase-contrast imaging up to this point. The x rays provided by conventional x-ray tubes do not have enough coherence for the interferometric method. But not all measurement methods for wave front aberrations correlating to phase-shift gradients are interferometric. Geometrical optics techniques may be used to measure ray aberrations [19]. Therefore, x-ray aberrations resulting from refraction can also be measured by use of geometrical optics methods without the coherence requirement. Thus, in this paper, we present an alternative method to obtain differential phase-contrast images under the incoherent condition with conventional x-ray sources.

II. PRINCIPLE

A. Coherent condition of Talbot interferometry

In current phase-contrast methods based on Talbot interferometry [20], ray deflection is measured by moiré metrology [12,21] or the phase-stepping approach [13,16], employing the combination of the self-imaging replica of the phase grating and the absorption grating at the fractional Talbot distance. According to the theory of the Talbot effect [22], a self-imaging phenomenon occurs when coherent x rays irradiate the phase grating whose period p is smaller than the transverse coherence length l_{coh} [13,16,25,26], that is,

$$l_{\text{coh}} \equiv \frac{L}{S}\lambda \geqslant p, \qquad (1)$$

where λ denotes the wavelength, S denotes the focal spot size of the source, and L denotes the distance between the source and the grating. This is the coherent condition of Talbot interferometry.

If the coherent condition is not satisfied, then the self-imaging phenomenon will disappear and Talbot interferometry will be invalidated. Synchrotron radiation sources and microfocus x-ray tubes are very appropriate for Talbot interferometry directly, but conventional x-ray tubes are just the

---

[*] huangzhifeng@mail.tsinghua.edu.cn

reverse. For example, suppose the small focal spot size of an x-ray tube is 170 μm and the average wavelength $\bar{\lambda}$ of the x rays is about 0.1 nm at 30 kV and 10 mA. A phase grating with a period of 2 μm should be placed at a distance of at least 3.4 m from the source to satisfy the coherent condition and produce the Talbot effect. It is very impractical for phase-contrast imaging with conventional x-ray tubes, so a source grating is placed close to the tube, and its openings must be narrow enough to provide partially coherent x rays for the Talbot effect. In the above case, if the openings of the source grating are smaller than 50 μm, the phase grating can be placed at a distance of 1.0 m from the source. Then the moiré effect is generated by the combination of the self-imaging replica of the phase grating and the absorption grating at the fractional Talbot distance. The visibility of moiré patterns has its maximal value contributed by each line source when the periods of the source grating p_0 and the absorption grating p_2 satisfy the condition [16]

$$p_0 = \frac{L_s}{D_T} p_2, \tag{2}$$

where L_s denotes the distance between the source grating and the phase grating, and D_T denotes the fractional Talbot distance between the phase grating and the absorption grating.

B. Moiré effect based on geometrical projection image

Moiré metrology is often applied to measure wave front aberration or ray deflection. The moiré effect can be produced by use of two absorption gratings separated by a distance when they are illuminated by light of any kind, including coherent and incoherent sources [21,23].

Suppose that an extended source $S(x,y)$ illuminates an absorption grating under the incoherent condition

$$l_{\mathrm{coh}} < p, \tag{3}$$

and a high-resolution detector is placed close to the grating. The geometrical projection image $I(x,y)$ of the grating is observed on the detector. It can be expressed by

$$I(x,y) = T(x,y) * S'(x,y), \tag{4}$$

where $T(x,y)$ denotes the image of the grating on the detector illuminated by a point source, and $S'(x,y)$ denotes the geometrical projection of the source on the detector. Furthermore,

$$S'(x,y) = S\left(-\frac{L}{D}x, -\frac{L}{D}y\right), \tag{5}$$

where D denotes the distance between the grating and the detector. Because of convolution processing, the projection image of the grating gets blurred as the detector is kept away from the grating (that is, D increases). When D exceeds a certain critical distance, the projection image will disappear.

Within the critical distance, the moiré effect can be generated by use of the combination of the first absorption grating's projection image and the second absorption grating. An experiment was performed to validate the moiré effect under the incoherent condition of $l_{\mathrm{coh}} < p$. An absorption grating with a period of 20 μm was placed at a distance of 1.02 m from the x-ray tube with a small focal spot size of 170 μm (30 kV p, 10 mA). It should be noted that the grating should be placed at a distance of more than 34 m from the tube when utilizing Talbot interferometry. A high-resolution x-ray charge-coupled device camera with 6.75 μm per pixel was placed behind the grating and recorded projection images of the grating at different distances. Line patterns in the projection images at different distances are plotted together for comparison, as seen in Fig. 1(a). It can be seen that the shapes of the grating were well retained at a distance of 86 mm while they were almost smoothed when the distance was more than 300 mm. The visibility of projection images declined as the distance increased, so the second absorption grating should be placed within the critical distance to produce the moiré effect with the projection image of the first grating.

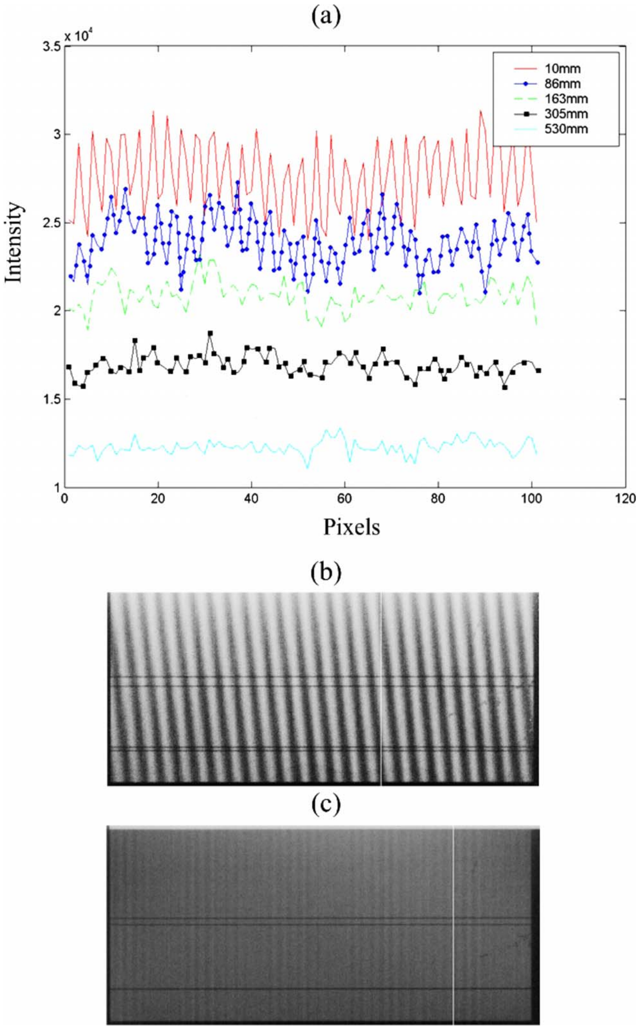

FIG. 1. (Color online) The experiment on the moiré effect under the incoherent condition. (The small focal spot size of the x-ray tube with 30 kV and 10 mA was measured to be 170 μm by a narrow slit.) (a) Line patterns in projection images at different distances for comparison. (b) Tilted moiré fringes. (c) Infinite moiré fringes.

Another absorption grating with a period of 22 μm was placed behind the first grating, and a PaxScan 2520 imager with a pixel pitch of 127 μm was utilized to capture the moiré effect. The periods of the moiré patterns are inversely proportional to the angle between the two gratings [23], so the periods of moiré patterns can be adjusted to be much larger than the grating period, even millimeters, and can be detected by the imager easily. The imager was placed close to the second grating to obtain more photon flux for this experiment. Tilted moiré fringes were observed naturally when the period of line patterns in the projection image of the first grating was not equal to the period of the second grating and the lines of the two gratings were not parallel to each other as shown in Fig. 1(b). Tilted moiré fringes disappeared and infinite moiré fringes [24] appeared when the lines of the two gratings were parallel to each other, and the distance D of the gratings was adjusted according to

$$\frac{p_1}{p_2} = \frac{L}{L+D}, \tag{6}$$

where p_1 and p_2 denote the periods of the first and second gratings, respectively. Infinite moiré fringes are shown in Fig. 1(c). Infinite moiré fringes are adopted to measure phase-shift gradients by the phase-stepping approach when the pixel pitch of the detector is larger than the period of the grating.

According to Eq. (4), the visibility of projection images is mainly influenced by the source size. If a source with a very large focal spot size irradiates the absorption grating, the critical distance will be very short. The projection image of the grating is hardly seen though the detector clings to the grating. As in Talbot-Lau interferometry, a source grating is also adopted in the case of a source with a large focal spot size under the incoherent condition. The main difference from Talbot-Lau interferometry is that the openings of the source grating do not need to be narrow enough to provide spatially coherent x rays for the Talbot effect, and thus more x rays can pass through the source grating and be utilized adequately in the experiment. In order to improve the visibility of projection images contributed by each small-focal-spot-size subsource split by the source grating, the period p_0 of the source grating should satisfy the condition

$$p_0 = m\frac{L_s}{D}p_2, \quad m = 1,2,3, \ldots . \tag{7}$$

Equation (7) is similar to Eq. (2) for Talbot-Lau interferometry.

C. Experimental setup under the incoherent condition

A phase-contrast imaging experiment setup under the incoherent condition is shown in Fig. 2. The phase-stepping approach with infinite moiré fringes produced by two absorption gratings (G_1 and G_2) is adopted to measure differential refractive index decrements of the tested object. In the case of the x-ray tube with a small focal spot size, phase-contrast images can be obtained directly by using two absorption gratings as seen in Fig. 2(a). In the case of the x-ray tube with a large focal spot size, a source grating corresponding to Eq. (7) is added in close proximity to the tube to provide an array of small-size subsources [shown in Fig. 2(b)].

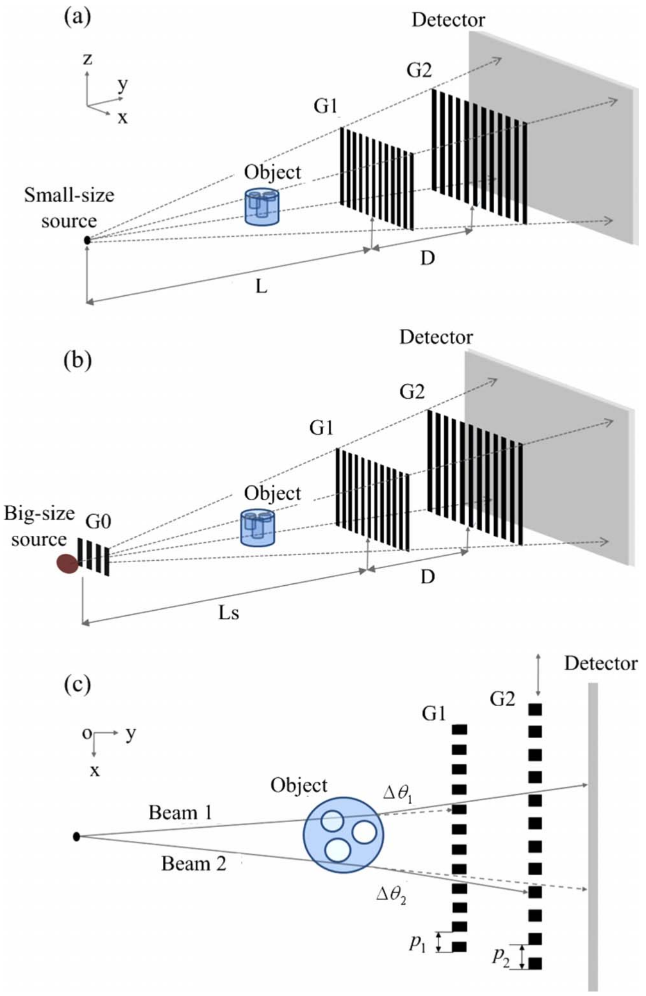

FIG. 2. (Color online) The hard x-ray phase-contrast imaging setup under the incoherent condition. (a) The case of a small-size source without a source grating. (b) The case of a large-size source with a source grating. (c) Two absorption gratings act as an optical gate to permit or forbid x rays from passing through during the phase-stepping approach.

Under the incoherent condition of $l_{\mathrm{coh}} < p_1$ utilized here, the x rays from the conventional tube or the source grating have weak coherence for diffraction, that is, little diffraction occurs when polychromatic x rays impinge upon the gratings. The result of this is that no Talbot effect exists. X-ray deflection measurements made by the phase-stepping approach can be explained from the viewpoint of geometrical optics. If two absorption gratings are placed perfectly parallel to each other, they act as an optical gate to permit or forbid the x rays from passing through as shown in Fig. 2(c). For example, in one step during the phase-stepping approach, if there is no object in the beam paths, beam 1 is blocked by G_1 and beam 2 passes through both gratings then it is captured by the detector. When beams 1 and 2 are both refracted slightly by the object, beam 1 is captured by the detector and beam 2 is blocked by G_2. In the next step, the reverse process perhaps occurs. The image of each step reflects x-ray refraction selected by these two gratings in different relative position.

The x-ray refraction phenomenon can be described by the refraction angle of the x ray refracted by the object. In theory, the refraction angle correlates to the differential refractive index decrement of the object [25]:

$$\Delta\theta = \int_{l:\text{path}(x,y)} \nabla\, \delta(x,y)dl, \tag{8}$$

where l:path(x,y) denotes the x-ray beam path passing through the object. Note that δ relates to the wavelength λ. This relationship can be written as

$$\delta \approx 1.350\,41 \times 10^{-6}\rho\lambda^2, \tag{9}$$

where ρ is the density of the object. Note that Eq. (9) is a simplified approximation showing the relation between density and wavelength. In phase-contrast methods based on Talbot interferometry, refraction angles are correlated with a certain wavelength that is selected to best satisfy the Talbot effect. X rays with other wavelengths from the x-ray tube may blur the results because their own Talbot distances are different. In our method under the incoherent condition, two absorption gratings act as an optical gate for x rays of all energy from the x-ray tube. The average refraction angles $\overline{\Delta\theta}$ are adapted to describe the holistic refraction effects of polychromatic x rays from the x-ray tube.

In the phase-stepping approach, several raw images are captured by the detector as the second grating is moved along the x axis step by step over one grating period. Each pixel of the detector has its own intensity oscillation over one grating period derived from the relative movement of the two absorption gratings [13]. If polychromatic x rays are refracted by the object before incidence upon a certain pixel, the intensity oscillation of this pixel will has a phase offset $\Delta\varphi$ relative to the background intensity oscillation without object. The average refraction angle can be calculated from

$$\overline{\Delta\theta} \approx \frac{p_2\Delta\varphi}{2\pi D}. \tag{10}$$

III. EXPERIMENTAL RESULTS

The experiments were carried out on an experimental setup at Tsinghua University. The target material of the x-ray tube was tungsten (W) and the inherent filtration was 0.8 mm beryllium (Be). The x-ray tube had two focal spot sizes: a small focal spot size, which was 170 μm with 30 kV and 10 mA, and a large focal spot size, which was 600 μm with 30 kV and 40 mA measured by a narrow slit. The average wavelength is estimated to be about 0.1 nm by the Monte Carlo method. A PaxScan 2520 imager detects x rays by use of a standard gadolinium oxysulfide (Gd_2O_2S) screen. The frame rate of the imager is 3.75 frames per second with 1536 rows and 1920 columns at a pixel pitch of 127 μm. Two sets of absorption gratings were used in the experiment: (1) Grating set 1: Two absorption gratings with large periods of 20 and 22 μm, respectively, an opening fraction of 0.5, and structure heights of absorption lines of 30 μm; (2) Grating set 2: Two absorption gratings with small periods of 10 and 11 μm, respectively, an opening fraction of 0.5, and structure heights of absorption lines of 20 μm.

An absorption grating with a period of 220 μm, openings of 50 μm, and structure heights of absorption lines of 40 μm acted as the source grating near the tube with a large focal spot size. That is to say, the grating closest to the souce split the large-sized source into an array of 50-μm-sized subsources.

A. Model sample

The experiments on a model sample were done in different modes under the incoherent condition: (1) Mode 1: The x-ray tube with a small focal spot size and grating set 1 without a source grating; (2) mode 2: The x-ray tube with a large focal spot size and grating set 1 with a source grating; (3) mode 3: The x-ray tube with a large focal spot size and grating set 2 with a source grating. The experimental parameters of these modes are listed in detail in Table I and the experimental results of the model sample are shown in Fig. 3.

The model sample consisted of two cylinders: the outer cylinder was made of polymethylmethacrylate and the inner cylinder was made of plastic. In each experimental mode, the phase-stepping approach with infinite moiré fringes was performed to calculate refraction-angle images $\overline{\Delta\theta}$ of the sample by measuring the phase offsets $\Delta\varphi$ of intensity oscillations over one grating period according to Eq. (10) on a pixel-by-pixel basis. There were 22 steps during the phase-stepping approach. For each step, 300 raw images were captured to reduce statistical and systematic noise. Finally, refraction-angle images of the sample in three experimental modes were obtained and are shown in Figs. 3(b)–3(d) for comparison. Severe x-ray refraction took place at the edges of the sample where large refractive index gradients existed. This led to large phase offsets $\Delta\varphi$ of the sample intensity oscillations (for example, pixel B) deviating from background intensity oscillations (for example, pixel A) as shown in Fig. 3(e). The contrast of the edges in the sample was enhanced sharply in all refraction-angle images. Among these refraction-angle images, the one of mode 1 had the most noise, while the one of mode 3 had the least noise and the most detailed structures. More noise existed in the refraction-angle image in mode 1 than the others because the current of the tube with a small focal spot size in mode 1 was four times lower than the current of the tube with a large focal spot size in other modes.

The spatial resolution in refraction-angle images is determined mainly by the source size, and therefore the refraction-angle image in mode 1 has the highest spatial resolution. The blurred edges of the sample can be observed in the refraction-angle images in modes 2 and 3. On the other hand, the contrast of refraction-angle images is dependent upon the ratio of the grating period to the distance between two gratings. For a determined distance between two gratings, the gratings with smaller periods can detect smaller phase shifts arising from slight x-ray refraction. Thus, the refraction-angle images in modes 1 and 2 have almost the

TABLE I. Experimental parameters in three modes.

Parameters	Mode 1	Mode 2	Mode 3
Focal spot size of the tube (μm)	170	600	600
Source grating	No	Yes	Yes
Size of the subsource (μm)	170	50	50
High voltage (kV)	30	30	30
Current (mA)	10	40	40
L or L_s (mm)	1601	1415	1415
D (mm)	160.1	141.5	141.5
l_{coh} for subsource (p_1 required) (μm)	0.94	2.83	2.83
p_1 (μm)	20	20	10
p_2 (μm)	22	22	11
Height of absorption lines (μm)	30	30	20
Step amount	22	22	22
Step interval (μm)	1.0	1.0	0.5

same contrast, while the refraction-angle image in mode 3 has the best contrast because the grating period utilized in mode 3 is two times smaller than the one used in modes 1 and 2. For example, the detailed structures marked by a circle can be distinguished in mode 3.

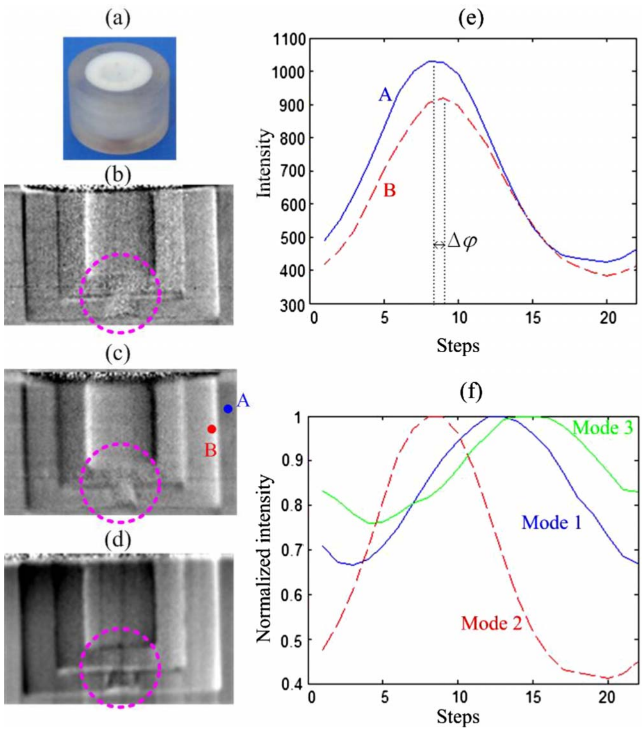

FIG. 3. (Color online) The experimental results of a model sample in different modes under the incoherent condition. (a) The photographic image. (b) The refraction-angle image obtained in mode 1. (c) The refraction-angle image obtained in mode 2. (d) The refraction-angle image obtained in mode 3. (e) The phase offset $\Delta\varphi$ of the sample intensity oscillation (pixel B) deviating from the background intensity oscillation (pixel A) over one grating period in the phase-stepping approach. (f) Normalized background intensity oscillations of three modes for comparison.

The visibility of the intensity oscillation in each mode can be calculated to be about 19%, 43%, and 15%, respectively, according to Fig. 3(f). The visibility of the intensity oscillation is mainly influenced by the source size and x-ray absorptivity of the grating. In the x rays with 30 kV, the gratings with structure heights of absorption lines of 30 μm have higher absorptivity than those of 20 μm. Comparing mode 1 with mode 2, it is found that the visibility of the intensity oscillation is increased by the source grating, but the contrast of the refraction-angle image is not enhanced.

B. Biological samples

We also applied mode 3 to inspect complicated biological samples (a wheat ear and a rice kernel in a small glass bottle) and the experimental result is shown in Fig. 4. The conventional radiographic image resulting from x-ray absorption was captured for comparison. The refraction-angle image has a different contrast representation from the conventional radiographic image and provides more detailed structures in the sample. For example, the shapes and structures of the wheat ear and the rice kernel can be observed very easily in the refraction-angle image while their misty shadows are hardly distinguishable in the conventional radiographic im-

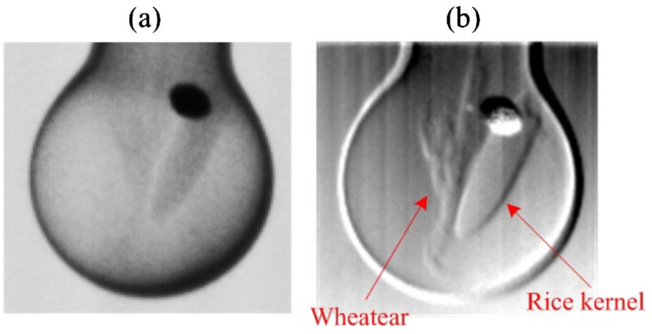

FIG. 4. (Color online) The experimental result for a complicated biological sample under the incoherent condition. (a) The conventional radiographic image. (b) The refraction-angle image.

age. This embodies the advantage of phase-contrast imaging over conventional radiography for weakly absorbing low-Z objects.

IV. CONCLUSION

The above experiments show that differential phase-contrast images can also be obtained with weakly coherent x rays under the incoherent condition of $l_{\mathrm{coh}} < p$. In some sense, the geometrical projection image of the first absorption grating under the incoherent condition plays the role of the self-imaging replica of the phase grating in Talbot interferometry under the coherent condition of $l_{\mathrm{coh}} \geqslant p$. Within a critical distance under the incoherent condition, the moiré effect can be generated by use of the combination of the first absorption grating's projection image and the second absorption grating. The phase-stepping approach with infinite moiré fringes is used to calculate refraction-angle images of the sample by measuring the phase offsets of intensity oscillations over one grating period on a pixel-by-pixel basis. The main difference in our method compared with Talbot interferometry is that the Talbot effect is not required so that the openings of the source grating for large-sized sources do not have to be narrow enough to provide partially spatially coherent x rays. More x rays can pass through the source grating and be utilized adequately in the experiment. Furthermore, the distance between the two gratings is not restricted by the Talbot distance and the period ratio determined by Eq. (6), so the choice of absorption gratings and the setup layout are relatively free. On the other hand, the distance between the source grating and the first absorption grating under the incoherent condition can be much shorter than the distance required by the Talbot effect. This means that the exposure time of the detector can be reduced. Certainly, the periods of the source grating and the second absorption grating are consequently altered to satisfiy experimental aims according to Eqs. (6) and (7). In conclusion, differential grating-based phase-contrast imaging can be realized under more relaxed conditions than before. Our method provides a feasible alternative approach to the practical application of phase-contrast imaging with conventional x-ray tubes under the incoherent condition. We believe that it will benefit clinical diagnoses, biological examinations, and material inspections in the near future.

ACKNOWLEDGMENTS

The authors thank Prof. Qunqing Li, Prof. Shuidi Wang, Prof. Yuxiang Xing, and Prof. Zheng Li at Tsinghua University, Prof. Heng Yang and Songtao Lu at Shanghai Institute of Microsystem and Information Technology, Prof. Peiping Zhu at the Institute of High Energy Physics, Chinese Academy of Sciences, for help and discussion. The work was supported by a grant from the National Natural Science Foundation of China (Grants No. 10875066 and No. 10575059) and by the Program for New Century Excellent Talents in University.

---

[1] A. G. Michette and C. J. Buckley, *X-Ray Science and Technology* (Institute of Physics Publishing, London, 1993).
[2] A. Momose, T. Takeda, A. Yoneyama, I. Koyama, and Y. Itai, Anal. Sci. **17**, 527 (2001).
[3] A. Momose, T. Takeda, and Y. Itai, Rev. Sci. Instrum. **66**, 1434 (1995).
[4] A. Snigirev, I. Snigireva, V. Kohn, S. Kuznetsov, and I. Schelokov, Rev. Sci. Instrum. **66**, 5486 (1995).
[5] S. W. Wilkins, T. E. Gureyev, D. Gao, A. Pogany, and A. W. Stevenson, Nature (London) **384**, 335–338 (1996).
[6] T. E. Gureyev, S. Mayo, S. W. Wilkins, D. Paganin, and A. W. Stevenson, Phys. Rev. Lett. **86**, 5827 (2001).
[7] T. J. Davis, D. Gao, T. E. Gueyev, A. W. Stevenson, and S. W. Wilkins, Nature (London) **373**, 595 (1995).
[8] D. Chapman *et al.*, Phys. Med. Biol. **42**, 2015 (1997).
[9] Z. Huang *et al.*, Appl. Phys. Lett. **89**, 041124 (2006).
[10] Z. Huang *et al.*, Appl. Phys. Lett. **91**, 011117 (2007).
[11] C. David, B. Nohammer, H. H. Solak, and E. Ziegler, Appl. Phys. Lett. **81**, 3287 (2002).
[12] A. Momose, S. Kawamoto, I. Koyama, and Y. Suzuki, Proc. SPIE **5535**, 352 (2004).
[13] T. Weitkamp *et al.*, Opt. Express **13**, 6296–6304 (2005).
[14] Y. Takeda, W. Yashiro, Y. Suzuki, S. Aoki, T. Hattori, and A. Momose, Jpn. J. Appl. Phys., Part 2 **46**, L89 (2007).
[15] M. Engelhardt *et al.*, Appl. Phys. Lett. **90**, 224101 (2007).
[16] F. Pfeiffer, T. Weitkamp, O. Bunk, and C. David, Nat. Phys. **2**, 258 (2006).
[17] F. Pfeiffer, C. Kottler, O. Bunk, and C. David, Phys. Rev. Lett. **98**, 108105 (2007).
[18] C. Kottler, F. Pfeiffer, O. Bunk, C. Grunzweig, and C. David, Rev. Sci. Instrum. **78**, 043710 (2007).
[19] J. David Briers, Opt. Lasers Eng. **32**, 111 (1999).
[20] S. Yokozeki and T. Suzuki, Appl. Opt. **10**, 1575 (1971).
[21] O. Kafri and I. Glatt, *The Physics of Moire Metrology* (Wiley, New York, 1990).
[22] H. F. Talbot, Philos. Mag. **9**, 403 (1836).
[23] O. Kafri, Opt. Lett. **5**, 555 (1980).
[24] O. Kafri, A. Livnat, and E. Keren, Appl. Opt. **21**, 3884 (1982).
[25] M. Born and E. Wolf, *Principles of Optics* (Pergamon, Oxford, 1980).
[26] J. Als-Nielsen and D. McMorrow, *Elements of Modern X-Ray Physics* (Wiley, New York, 2001).